Studies on Temperature and Strain Sensitivities of a Few-mode Critical Wavelength Fiber Optic Sensor

Chenxu Lu, Juan Su, Xiaopeng Dong, Lihua Lu, Tong Sun and Kenneth T. V. Grattan

***Abstract*— This paper studied the relationship between the temperature/strain wavelength sensitivity of a fiber optic in-line Mach-Zehnder Interferometer (MZI) sensor and the wavelength separation of the measured wavelength to the critical wavelength (CWL) in a CWL-existed interference spectrum formed by interference between LP_{01} and LP_{02} modes. The in-line MZI fiber optic sensor has been constructed by splicing a section of specially designed few-mode fiber (FMF), which support LP_{01} and LP_{02} modes propagating in the fiber, between two pieces of single mode fiber. The propagation constant difference, $\Delta\beta$, between the LP_{01} and LP_{02} modes, changes non-monotonously with wavelength and reaches a maximum at the CWL. As a result, in sensor operation, peaks on the different sides of the CWL then shift in opposite directions, and the associated temperature/strain sensitivities increase significantly when the measured wavelength points become close to the CWL, from both sides of the CWL. A theoretical analysis carried out has predicted that with this specified FMF sensor approach, the temperature/strain wavelength sensitivities are governed by the wavelength difference between the measured wavelength and the CWL. This conclusion was seen to agree well with the experimental results obtained. Combining the wavelength shifts of the peaks and the CWL in the transmission spectrum of the SFS structure, this study has shown that this approach forms the basis of effective designs of high sensitivity sensors for multi-parameter detection and offering a large measurement range to satisfy the requirements needed for better industrial measurements.**

Chenxu Lu is with the Institute of Lightwave Technology, School of Information Science and Technology, Xiamen University, Xiamen, Fujian 361005, China, and is with the School of Mathematics, Computer Science and Engineering, City, University of London, Northampton Square, London, EC1V 0HB, United Kingdom. (e-mail: chenxvlu0129@stu.xmu.edu.cn).

Juan Su is now with the Institute of Marine Science and Technology, Shandong University, Jinan, Shandong 250100, China. She was pursuing the doctoral research in the Institute of Lightwave Technology, School of Information Science and Technology, Xiamen University, Xiamen, Fujian 361005, China, during the completion of this work. (e-mail: sujuan@sdu.edu.cn).

Corresponding author Xiaopeng Dong is with the Institute of Lightwave Technology, School of Information Science and Technology, Xiamen University, Xiamen, Fujian 361005, China. (e-mail: xpd@xmu.edu.cn).

Lihua Lu is with the Institute of Lightwave Technology, School of Information Science and Technology, Xiamen University, Xiamen, Fujian 361005, China. (e-mail: lihualu@stu.xmu.edu.cn).

Tong Sun is with the School of Mathematics, Computer Science and Engineering, City, University of London, Northampton Square, London, EC1V 0HB, United Kingdom. (e-mail: t.sun@city.ac.uk).

Kenneth T. V. Grattan is with the City Graduate School and the School of Mathematics, Computer Science and Engineering, City, University of London, Northampton Square, London, EC1V 0HB, United Kingdom. (e-mail: K.T.V.Grattan@city.ac.uk).

***Index Terms*—In-line Mach-Zehnder interferometer, few mode fiber, critical wavelength, strain sensitivity, temperature sensitivity.**

I. Introduction

FIBER optic in-line Mach-Zehnder Interferometers (MZIs), which are normally formed by two modes interference between the fundamental core mode, LP_{01} and the high order core modes [1], the cladding modes [2] or another fundamental core mode LP_{01} from a different core [3] (in a fiber of such multicore design), have been widely investigated in recent years. With advantages of their high sensitivity, immunity to electromagnetic interference, compact size and durability in harsh and corrosive environments, the in-line MZIs based on two modes interference have been applied to various industrial circumstances, such as structural health monitoring, earthquake monitoring and manufacturing, for example [4-6]. For most reported in-line MZIs based on two modes interference, because the propagation constant difference between two interference modes change linearly with wavelength, the interference fringes, which have been seen in the transmission spectra, change periodically and the peaks/dips shift in the same wavelength direction under different strain or temperature variations [1-3,7]. However, in some modal interferometers based on the interference between the fundamental core mode, LP_{01}, and the first circularly symmetric higher-order core mode, LP_{02}, a critical wavelength (CWL) exists in the transmission spectra, and the wavelength spacing between adjacent peaks reach a maximum for the peak that closest to CWL on each side. As reported in the references [8-15], in the CWL-existed in-line MZIs constructed by single mode fiber (SMF) – GeO_2-doped graded-index multimode fiber (MMF) – single mode fiber (SMS) structure [8, 9], or SMF – few mode fiber (FMF) – SMF (SFS) structure [10-15], the peaks on the different sides (both the lower wavelength side and the higher wavelength side) of the CWL shift to opposite wavelength directions under conditions where temperature or strain variations are seen, and the temperature/strain sensitivity reaches a maximum for the peak that located closest to the CWL (one from each side). However, all the previous studies have been focused on the analysis of the CWL behavior [11-14] and only the experimental behaviors of the peaks are studied [15]. The temperature/strain sensitivities of the interference fringes and the relationship between the temperature/strain sensitivities of

the measured wavelengths and the wavelength spacing of the measured wavelengths to the CWL have not been studied in detail, either theoretically or experimentally. The work reported here forms the basis of a better understanding of the potential performance of a sensor based on exploiting this phenomenon fully.

Thus in this paper, the temperature/strain characteristics of a SFS-structured in-line MZI employing a specially designed FMF were theoretically analyzed, their performance predicted and this experimentally demonstrated. Both theoretical and experimental results show that, the temperature/strain sensitivities of the device increase significantly as the wavelengths approaching the CWL from both sides, and with the certain fiber structure and refractive index parameters, the temperature/strain sensitivities of the device are only governed by the wavelength spacing between the measured wavelength and the CWL. Under different temperature/strain conditions, the temperature/strain sensitivities at a series of wavelengths in the transmission spectra of the SFS structure employing a 30cm, 40cm and 50cm FMF were measured in the experiments, and the results agree well with the simulation, giving confidence in the design. The temperature/strain sensitivity study in this paper provide an approach for improving temperature and strain sensitivities of SFS structure-based sensors, by detecting peaks in the transmission spectrum. Further, by tracking the wavelength shifts of both the CWL and the peaks in the transmission spectrum when the system is perturbed, the SFS structure discussed can be applied to the development of simple and co-located multi-parameter sensors. These could be made available at low cost and which have practical applications in various industrial processes.

II. Theoretical Analysis of the SFS Structure

The in-line MZI sensor that can be constructed by employing the SFS approach is formed, as shown in Fig. 1(a), by splicing a piece of FMF and placing it between two pieces of SMF. The FMF used in the experiments are provided by Yangtze Optical Fiber and Cable Joint Stock Limited Company. A scanning electron microscope (SEM) micrograph of the FMF used in the experimental verification is shown in Fig. 1(b). The geometrical structure and the relative index difference profile (at a wavelength of 670nm) of FMF used in the simulation are shown in Fig. 2. The relative refractive index difference is defined as $\Delta n_{co/cli} = (n_{co/cli} - n_0)/n_0$, where the $n_{co/cli}$ and n_0 are the refractive indices of the core/ith inner cladding and pure silica of the FMF, respectively. The FMF is specially designed with five layers: a core region with a positive high refractive index Δn_{co} (GeO_2-doped ridge); a first inner cladding region with a negative refractive index Δn_{cl1} (F-doped trench); a second inner cladding region with a positive refractive index Δn_{cl2} (GeO_2-doped ridge); the third inner cladding region with a positive refractive index Δn_{cl3} (GeO_2-doped ridge, $\Delta n_{co} > \Delta n_{cl2} > \Delta n_{cl3}$); and a pure SiO_2 outer cladding. With the multi-layer geometrical structure and W-shaped refractive index difference profile, at the operational wavelength planned, the fiber supports the fundamental core mode, LP_{01}, and does not support the LP_{11} mode, but does support the first circularly symmetric high order core mode, LP_{02}, propagating in the fiber [16]. Using the finite element analysis method [17, 18], the simulated mode field distributions of the propagating core modes (at a wavelength of 1550nm), LP_{01} and LP_{02}, are shown in Fig. 1(c) and (d), respectively.

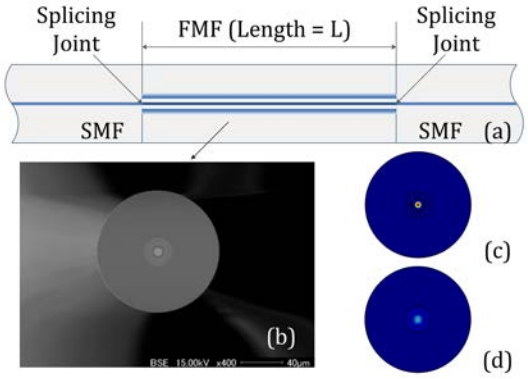

Fig. 1. (a) Diagram of the SMF-FMF-SMF (SFS) structure. (b) The SEM micrograph of the FMF. (c) The simulated mode field distribution of the propagating LP_{01} mode in the FMF. (d) The simulated mode field distribution of the propagating LP_{02} mode in the FMF. SMF – Single Mode Fiber; FMF – Few Mode Fiber.

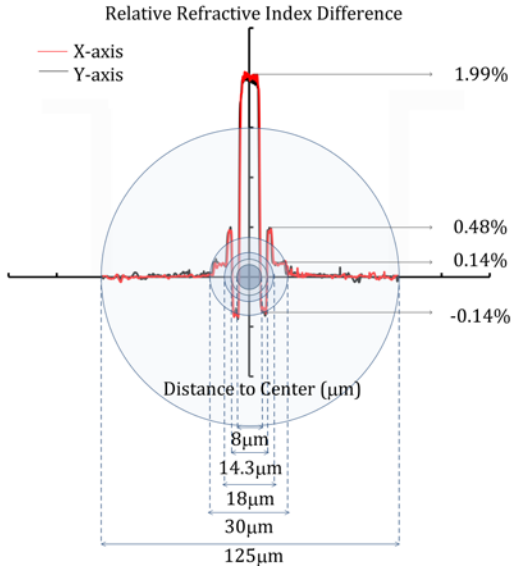

Fig. 2. Geometrical structure and refractive index difference profile (@670nm) of the few mode fiber (FMF). The parameters used in the simulation are: d_{co}=8μm, Δn_{co}=1.99%, d_{cl1}=14.3μm, Δn_{cl1}= –0.40%, d_{cl2}=18μm, Δn_{cl2}=0.48%, d_{cl3}=30μm, Δn_{cl3}=0.14%.

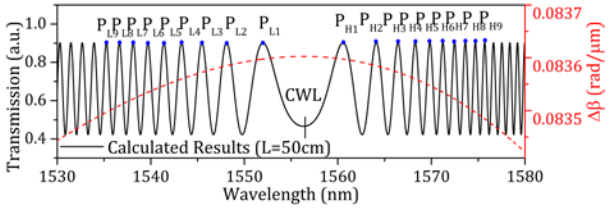

Fig. 3. Calculated $\Delta\beta$ vs. wavelength and simulated transmission spectrum of the SFS structure with unstrained FMF under temperature of 25°C (L=50cm).

In the SFS sensor structure, the LP_{01} and LP_{02} modes propagating in the FMF are excited by the fundmental core mode, LP_{01}, in the input SMF. The interference between the LP_{01} and LP_{02} modes is selected by using the output SMF. If the optical power ratios transferred to the LP_{01} and LP_{02} modes from the input SMF are $t_1=P_1/P_{in}$ and $t_2=P_2/P_{in}$, respectively, then the transmission through the FMF is simply given by [10]:

$$T=P_{out}/P_{in}=t_{01}^2+t_{02}^2+2t_{01}t_{02}\cos\left(\varphi(\lambda)\right) \quad (1)$$

where $\varphi(\lambda)$ is the phase difference developed between the LP_{01} and LP_{02} mode in the FMF forming the basis of the sensor with the physical length of L, which is represented by:

$$\varphi(\lambda)=\Delta\beta(\lambda)\cdot L \quad (2)$$

where $\Delta\beta=\beta_{01}-\beta_{02}=\frac{2\pi\Delta n_{eff}}{\lambda}$ is the propagation constant difference between the LP_{01} and LP_{02} modes, and β_{01} and β_{02} are the propagation constants of the LP_{01} and LP_{02} modes in the FMF, respectively. Δn_{eff} is the effective index difference between the LP_{01} and LP_{02} modes. With the fiber parameters given in Fig. 2, using the finite element analysis method, the simulated relationship between $\Delta\beta$ and the wavelength (at a temperature of 25℃) without axial strain, is depicted as a dashed line in Fig. 3. The calculated transmission spectrum combining Equation (1) and the simulated value of $\Delta\beta$ is shown as a solid line in Fig. 3, where the physical length of the FMF employed is 50cm. In Fig.3, the calculated CWL for a straight FMF at a temperature of 25℃ is 1556.20nm, which coincides well the experimental value of 1556.22nm. Due to the fact that at the operational wavelength, the dispersion of $\Delta\beta$ exhibits non-linear behavior and has a maximum, corresponding to the value of the CWL in the transmission spectrum, the periods of interference fringes closest to the CWL from both sides reach a maximum. As shown in Fig. 3, numbering from the peaks that lie closest to the CWL from both sides, the peaks that are located on the higher wavelength side of CWL (i.e., within the region from CWL to 1580nm) are denoted as P_{H1}, P_{H2}, ..., respectively. Peaks that are located on the lower wavelength side of CWL (i.e., within the region from 1530nm to CWL) are denoted as P_{L1}, P_{L2}, ..., respectively.

III. Temperature Sensitivies of Peaks

Because the phase difference between the LP_{01} and LP_{02} modes in the sensor is a function of both the operational wavelength, λ, and the perturbation parameter, χ (temperature or strain), as shown in Equation (2). When the whole length of the FMF, L, acts as the sensing element, the change in the phase difference can be written as [8]:

$$\Delta\varphi=\frac{\partial\varphi}{\partial\lambda}\Delta\lambda+\frac{\partial\varphi}{\partial\chi}\Delta\chi \quad (3)$$

where $\Delta\chi$ represents temperature variations, ΔT, or strain induced elongations, ΔL. For a constant phase point ($\Delta\varphi=0$), the following is given:

$$\frac{\Delta\lambda}{\Delta\chi}=-\frac{1}{L}\left(\frac{\partial\varphi}{\partial\chi}\right)\left(\frac{\partial(\Delta\beta)}{\partial\lambda}\right)^{-1} \quad (4)$$

When the temperature of the FMF change by ΔT, Equation (4) can be written as:

$$\frac{\Delta\lambda}{\Delta T}=-\frac{1}{L}\left(\frac{\partial\varphi}{\partial T}\right)\left(\frac{\partial(\Delta\beta)}{\partial\lambda}\right)^{-1} \quad (5)$$

where $\frac{\partial\varphi}{\partial T}$ is the change of φ with respect to the per degree change of temperature. As both L and $\Delta\beta$ change simultaneously with the variation in temperature, $\frac{\partial\varphi}{\partial T}$ is given by [19]:

$$\frac{\partial\varphi}{\partial T}=\frac{\partial(\Delta\beta L)}{\partial T}=\frac{\partial(\Delta\beta)}{\partial T}+\Delta\beta(\alpha L) \quad (6)$$

where $\alpha=\frac{1}{L}\frac{\partial L}{\partial T}=5.1\times10^{-7}/°C$ is the thermal expansion coefficient for pure silica. To calculate Equation (6), the simulated value of $\Delta\beta$ at temperatures of 25℃, 35℃, 45℃, 55 ℃, 65 ℃ and the values of $\partial(\Delta\beta)/\partial T$ as a function of wavelength are calculated and depicted in Fig. 4.

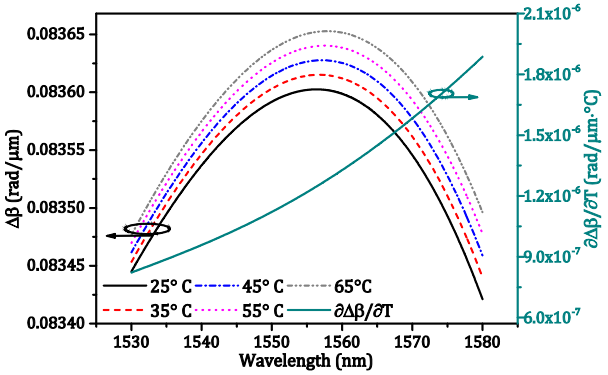

Fig. 4. Simulated results of $\Delta\beta$ under different temperatures and $\partial(\Delta\beta)/\partial T$ with wavelength.

Combing Equations (5) and (6), the temperature wavelength senstivitiy of the peaks, $\Delta\lambda/\Delta T$, as a function of wavelength, is thus given by Equation (7). As shown in Equation (7), with specified fiber parameters and structures shown in Fig. 2, the remained terms, $\partial(\Delta\beta)/\partial T$, $\Delta\beta$, and $\frac{\partial(\Delta\beta)}{\partial\lambda}$ in (7) are only related to the wavelength. The calculated $\Delta\lambda/\Delta T$ as a function of the normalized wavelength (defined as λ/λ_{CWL}) is depicted in the Fig. 9 as a solid line, together with the experimental results.

$$\frac{\Delta\lambda}{\Delta T}=-\left(\frac{\partial\Delta\beta}{\partial T}+\Delta\beta\cdot\alpha\right)\left(\frac{\partial(\Delta\beta)}{\partial\lambda}\right)^{-1} \quad (7)$$

To verify the temperature sensitivity simulation discussed above, three SFS (SMF-FMF-SMF) sensor structures with

FMF physical lengths of 30cm, 40cm, 50cm were explored in the experiments carried out. The SFS sensors are formed by spicing a piece of FMF between two sections of standard SMF (Coring SMF-28e). The transmsion spectra of three free SFS structures at room temperature are shown in Fig. 5. Because peaks are easy to identify and monitor in the interference spectra, the temperature senstivities of the proposed SFS structure are fully explored in the experiments by investigating the wavelength shifts of 18 peaks in the transmission spectra of each SFS sturcture: P_{L1}, P_{L2}, ..., P_{L9}, and P_{H1}, P_{H2}, ..., P_{H9}, around temperatures of 25℃ and 60℃.

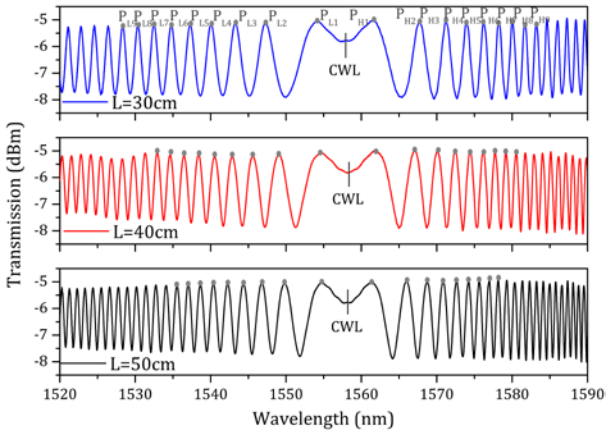

Fig. 5. Transmission spectra of the SFS structures employing 30cm, 40cm, 50cm length of FMF under room temperature (T= 25℃).

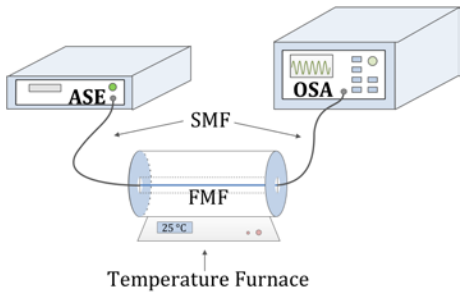

Fig. 6. Experimental setup of temperature sensitivity measurement based on the SFS sensor structure. ASE – Amplified Spontaneous Emission Source; OSA – Optical Specrtum Analyzer; SMF – Single Mode Fiber; FMF – Few Mode Fiber.

The schematic diagram of the experimental setup used to measure the temperature senstivity of the SFS sensor device is shown in Fig. 6. To study the effect of temperature, the FMF section was passed through a temperature furnace. Light was launched into the SFS structure using an Er-doped amplified spontaneous emission (ASE) broadband light source over a wavelength range of 1520nm to 1600nm, and the transmission spectra were recorded by use of an Optical Spectrum Analyzer (OSA, AQ6317B – with a wavelength accuracy of 0.02 nm). The transmission spectra of the SFS structure with 50cm length of FMF at temperatures of 58.05℃, 60.08℃, and 61.04℃ are shown in Fig. 7. The wavelength shifts of P_{L1}, ..., P_{L9}, and P_{H1}, ..., P_{H9}, around the temperature of 60℃ with the 50cm length FMF are shown in Fig. 8 (a) and (b), respectively. As shown in both Fig. 7 and Fig. 8, the peaks on each side of the CWL shift in opposite directions, and P_{L1} and P_{H1} exhibits much larger shifts than other peaks. As the wavelength spacing between peaks and the CWL becomes larger, the temperature sensitivity becomes a constant.

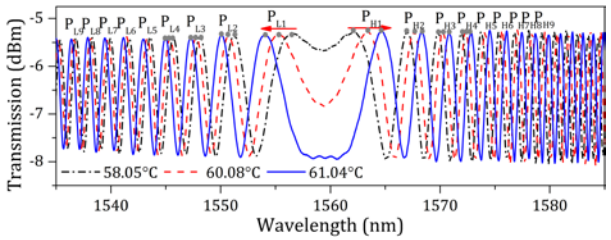

Fig. 7. The transmission spectra of the SFS sturcture under temperature of 58.05℃, 60.08℃, and 61.04℃ with the FMF physical length of 50cm.

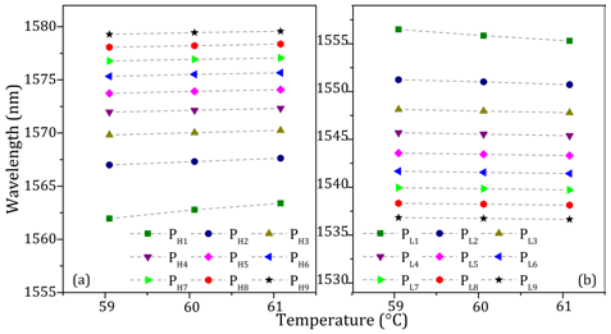

Fig. 8. Wavelength shifts of peaks in the transmission spectra of the SFS sensor from the temperature sensing system with the FMF physical length of 50cm.

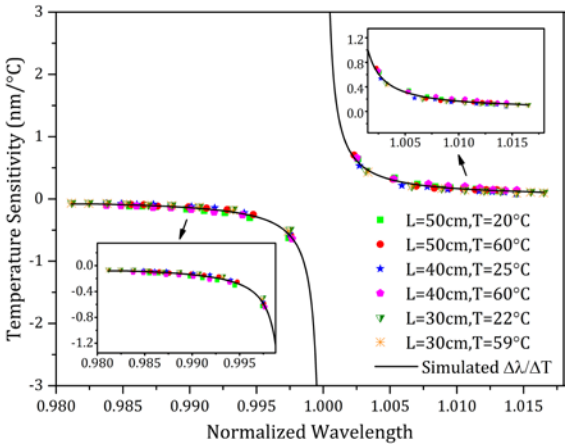

Fig. 9 The simulated and experimental temperature sensitivity of the SFS structure vs. the normalized wavelength.

The experimental temperature sensitivties v.s the normalized wavelength of the SFS sensor device employing different lengths of FMF (30cm, 40cm, and 50cm), measured around temperature of 25℃ and 60℃, are plotted in Fig. 9, and agree well with the simulated results. As shown in Fig. 9, the temperature sensitivity of the measured wavlength (here are 18 peaks in the transmission spectrum) is only related to the wavelength spacing of the measured wavelength to the CWL. The physical length of the FMF used in the SFS sensor and the temperature applied to the FMF section may change the wavelength seperation between the peak wavelength and the CWL, in return, affect the corresponding temperature sensitivity of the measured peak wavelength. As the peak wavelength value approaching the CWL value ($\lambda/\lambda_{CWL} \to 1$),

because the value of $\partial(\Delta\beta)/\partial\lambda$ in Equation (7) reaches zero, the temperature sensitivity increase significantly, as shown in Fig. 9, from both the theoretical and experimental points of view. However, the mathematical-derived infinitely high strain or temperature sensitivity at the CWL has no practical meaning, because $\partial(\Delta\beta)/\partial\lambda = 0$ at the CWL from the theoretical analysis, and infinite length of FMF is needed in experiments to minimize the wavelength spacing between the wavelength of P_{L1}/P_{H1} and the CWL, which is unpractical in applications.

IV. Strain Sensitivies of Peaks

In the strain sensor formed by the SFS structure, if the FMF section is strained longitudinally at a constant temperature with a change of length, ΔL, occurring, Equation (4) can be written as:

$$\frac{\Delta\lambda}{\Delta\varepsilon} = -\frac{\partial\varphi}{\partial L}\left(\frac{\partial(\Delta\beta)}{\partial\lambda}\right)^{-1} \tag{8}$$

where $\Delta\varepsilon=\Delta L / L$ is the variation of the axial strain. $\partial\varphi/\partial L$ is the change in phase difference produced by per unit increase in the physical length of the FMF. Using the following equation given in [20]:

$$\frac{\partial\varphi}{\partial L} = \Delta\beta + \frac{k_0^2}{2\beta_{01}\beta_{02}}\cdot\left\{\gamma\left[n_0^4\Delta\beta + \left(n_{co}^4 - n_0^4\right)\cdot\left(\beta_{01}b_{01} - \beta_{02}b_{02}\right)\right] + V\delta\left[\beta_{01}\frac{\partial b_{01}}{\partial V} - \beta_{02}\frac{\partial b_{02}}{\partial V}\right]\right\} \tag{9}$$

where $\gamma=p_{12}-\sigma\left(p_{11}+p_{12}\right)$, $\delta=\sigma(n_{co}^2-n_0^2)+\frac{\gamma}{2}(n_{co}^4-n_0^4)$, p_{11} and p_{12} are strain-optic coefficients for fused silica (0.12 and 0.27, respectively), σ=0.17 is the Poisson ratio. $k_0 = 2\pi/\lambda$ is the free space wave vector. $V=k_0\left(d_{co}/2\right)\sqrt{n_{co}^2-n_0^2}$ is the normalized frequency of the FMF. b_{0i} (i=1,2) is the normalized propagation constant, and is represented as:

$$\beta_{0i}^2 = k_0^2\left[n_0^2 + b_{0i}\left(n_{co}^2 - n_0^2\right)\right] \tag{10}$$

Given the cross-sectional parameters and the refractive index difference profile of the FMF sensor device presented in Fig. 2, the calculated value of $\partial\varphi/\partial L$ as a function of wavelength is shown in Fig. 10. By combining Equations (8), (9), and (10), the strain sensitivity of peaks, $\Delta\lambda/\Delta\varepsilon$, can be written as a function of wavelength:

$$\frac{\Delta\lambda}{\Delta\varepsilon} = -\left\{\begin{array}{l}\Delta\beta + \dfrac{k_0^2}{2\beta_{01}\beta_{02}}\cdot \\ \left\{\gamma\left[\begin{array}{l} n_0^4\Delta\beta + \left(n_{co}^4 - n_0^4\right)\cdot \\ \left(\beta_{01}b_{01} - \beta_{02}b_{02}\right)\end{array}\right]\right. \\ \left. + V\delta\left[\beta_{01}\dfrac{\partial b_{01}}{\partial V} - \beta_{02}\dfrac{\partial b_{02}}{\partial V}\right]\right\}\end{array}\right\}\left(\frac{\partial(\Delta\beta)}{\partial\lambda}\right)^{-1} \tag{11}$$

Using the simulated value of $\Delta\beta$ in Fig. 3 and $\partial\varphi/\partial L$ in Fig. 10, the simulated strain sensitivity of peaks, $\Delta\lambda/\Delta\varepsilon$, as a function of the normalized wavelength is depicted as the solid line in Fig. 13, together with the experimental results also obtained.

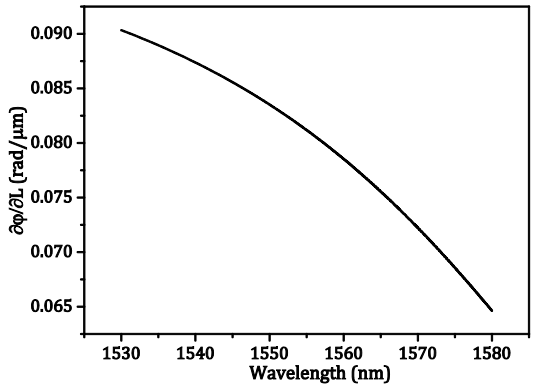

Fig. 10. The calculated relationship between $\partial\varphi/\partial L$ of the FMF with wavelength.

Similar as the temperature sensors, the SFS strain sensors formed with the FMF physical lengths of 30cm, 40cm, 50cm are employed to verfied the simulation results. The schematic diagram of the experimental setup is shown in Fig. 11. For axial strain measurement, the input SMF was mounted on a fixed stage and the output SMF was spliced to a Fiber Bragg Grating (FBG) strain sensor. The grating period and grating length of the FBG strain sensor used in the experiment are 526.64nm and 8mm, respectively, with the strain sensitivity of 1.2pm/με [21]. One side of a spring was fixed to the translation stage and the other side was spliced to the pigtail of the FBG. As the translation stage moves, the same axial strain was applied to both the FMF and FBG. In this case, the axial strain applied to the FMF section can be measured by detecting the Bragg wavelength shift of the FBG. The strain sensitivities were measured at a constant (room) temperature.

As the translation stage moves, the axial strain applied to the FMF increases. Figure 12 (a) and (b) show the wavelength shifts of P_{L1}, ..., P_{L9}, and P_{H1}, ..., P_{H9} in the transmission spectra of the SFS strain sensor employing a 50cm length of FMF, around the axial strain of 150με, respectively. As shown in Fig. 12, with the axial strain applied to the FMF increases, the peaks on the lower wavelength side of the CWL, i.e., P_{L1}, ..., P_{L9}, show blue shifts; conversely, the peaks on the higher wavelength side of the CWL, i.e., P_{H1}, ..., P_{H9}, show red shifts. The experimental strain senstivities of the measured peaks in the transmission spectra of the SFS structured strain sensors employing 30cm, 40cm, 50cm length of FMF are plotted together with the simulated results in Fig 13. The strain sensitivity of peaks increase significantly as the peak wavelength approaching the CWL, while remain constant as the wavelength spacing between peaks and the CWL become large.

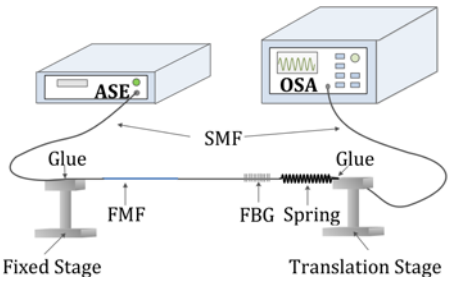

Fig. 11. Experimental setup of strain sensitivity measurement based on the SFS structure. ASE – amplified spontaneous emission source; OSA – Optical Specrtum Analyzer; SMF – Single Mode Fiber; FMF – Few Mode Fiber; FBG – Fiber Bragg Grating.

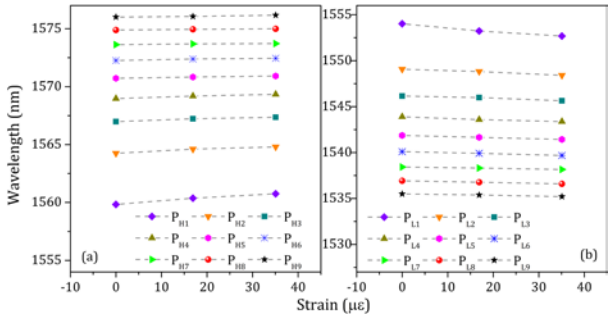

Fig. 12. Wavelength shifts of peaks in the transmission spectra of the SFS sensor from the strain sensing system with the FMF physical length of 50cm.

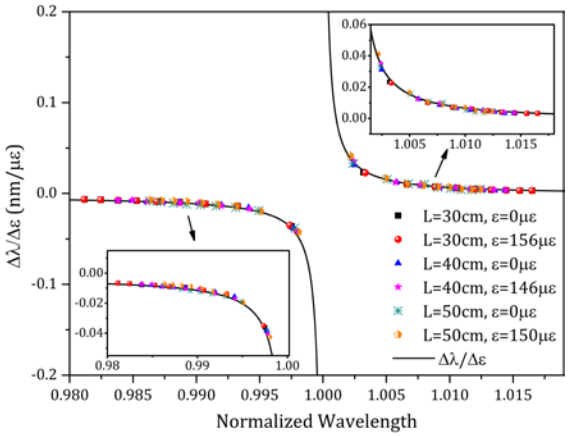

Fig. 13 The simulated and experimental strain sensitivity of the SFS structure vs. the normalized wavelength.

V. DISSCUSSION

When the whole length of the FMF acts as a sensing element in a SFS sensor device constructed, the results, both theoretical and experimental seen in Fig. 9 and Fig. 13 show that the strain and temperature sensitivities of such a SFS structure are independent of the physical lengths of the FMF used in the sensor. Moreover, with the geometrical structure and relative refractive index difference profile of the FMF given in Fig. 1 in Section II, the strain/temperature sensitivity of a specific peak is governed by the wavelength separation between the peak wavelength and the CWL. The wavelength separation between the two interference maxima (the Free Spectral Range, FSR) can be deduced from the Equation (1) and (2), and approximated as:

$$\Delta\lambda \approx \frac{\lambda^2}{\Delta n_{eff} L} \tag{12}$$

Therefore, by increasing the physical length, *L*, of the FMF used in the sensor structure, it can be seen from Equation (12) that the FSR will decrease, and the wavelength seperation between peak wavelengths (i.e. P_{L1} and P_{H1}) and the CWL get smaller, as seen in Fig. 5. In this case, as seen in Fig. 9 and Fig. 13, in the experimental application of the SFS structured temperature or strain sensors, the sensitivity performance of the sensors can be improved by increase the physical length of the FMF used in the SFS structure, especially for the sensors based on the peak wavelength detection of P_{L1} and P_{H1}.

A. Temperature and strain sensors based on peak detections

Based on the temperature and strain sensitivitiy study shown in Section III and IV, the peaks, P_{L1} and P_{H1}, in the transmission spectrum of SFS structure exhibit high temperature and strain sensitivies as their wavelengths approaching the CWL. Thus this can signal a sensitivity of -0.586 nm/°C, and 0.704 nm/°C for temperature measurement, and a sensitivity of -0.043nm/με and 0.041nm/με for strain measurement (where L=50cm for FMF), respectively, or even higher sensitivites if the locations of the peaks (i.e. P_{L1} and P_{H1}) become closer to the CWL, by increasing the length of the FMF section. However, when the wavelength seperations between the peaks and the CWL become large in the transmission spectrum, peaks linearly shift with temperature or strain variations. Using the linear strain and temperature sensitivities of the peaks, a simple, co-located, high-resolution sensing structure for the simultaneous discrimination of strain and temperature can be developed, as reported by Lu et al [15].

Besides, the SFS structure can also be developed into a compact strain/temperature sensor with the merits of high sensitivity, polarization-independence and low cost, when the initial peak wavelength is adjused to be close to the CWL. The comparison between the simulated performance of the proposed SFS sensor device in this study and the reported in-line MZI-based strain/temperature sensors is shown in Table I.

TABLE I
QUANTITATIVE COMPARISON OF STRAIN AND TEMPERATURE SENSITIVITIES OF SEVERAL REPORTED SCHEMES

Ref.	Interference Modes	Strain Sensitivity (pm/με)	Temperature Sensitivity (pm/°C)
[1]	LP_{01} mode and another unknown high order core mode	18.6	58.5
[2]	LP_{01} mode and cladding mode	Not given	88
[3]	LP_{01} modes coming from different cores	0.284	130.6
This study	LP_{01} and LP_{02} modes	43	704

B. Large strain and temperature measurement range sensors with enhanced sensitivites based on the CWL and peak wavelength detection.

In a way similar to all in-line MZI-based sensors, the peak

wavelength detection method may suffer from a limited measurement range and confusion due to a multi-value problem because it is difficult to identify and follow one specific peak from periodically changed interference fringes. As shown in the previous studies, the CWL in the transmission spectrum of the SFS structure is exclusive, easy to identify and monotonically shift in the transmission spectrum with a strain sensitivity of 0.001nm/με and a temperature sensitivity of 0.042nm/℃ at the operation wavlength [11-15]. By combining both characteristics of the CWL and the peaks in the transmission spectrum of the SFS structure, strain or temperature sensor designs with large measurement range and enhanced sensitivity can be expected, which gives good monitoring prospects in many practical applications, such as health monitoring of civil structures and situations where temperture compensation is required [22].

VI. Conclusion

This paper has presented a comprehensive study on the strain and temperature sensitivities of the peaks in the transmission spectrum of an in-line MZI-based fiber optic sensor using the interference between the LP_{01} and LP_{02} modes. Both the theoretical analysis and the experimental results show that with the specific FMF used in the paper, the strain and temperature sensitivities of the peaks in the transmission spectrum of the sensor are governed by the wavelength spacing between the peak wavelength and the CWL. By choosing the appropriate peaks in the transmission spectrum, the basic SFS structure can be designed as several different kind of sensors, that can be configured to satisfy the range of practical applications possible.

Acknowledgment

The authors would like to thank Yangtze Optical Fiber and Cable Joint Stock Limited Company for providing the FMF used in the experiment. Financial support from the National Natural Science Foundation of China (Project no. 61775186); the Fujian Provincial Department of Science and Technology (Project no. 2014H6027); the Marine and Fisheries Bureau of Xiamen (Project no. 16CZB025SF03); and Bureau of Science and Technology of Quanzhou (Project no. 2015G32) are gratefully acknowledged. The support of the Royal Academy of Engineering and the George Daniels Educational Trust are greatly appreciated.

References

[1] Y. Liu, L. Wei, "Low-cost high-sensitivity strain and temperature sensing using graded-index multimode fibers", *Appl. Opt.*, vol. 46, no. 13, pp. 2516-2519, May 2007.

[2] L. V. Nguyen, D. Hwang, S. Moon, D. S. Moon, Y. Chung, "High temperature fiber sensor with high sensitivity based on core diameter mismatch", *Opt. Express*, vol. 16, pp. 11369-11375, 2008.

[3] Z. Zhao et al., "All-solid multi-core fiber-based multipath Mach–Zehnder interferometer for temperature sensing", *Appl. Phys. B*, vol. 112, no. 4, pp. 491-497, Sep. 2013.

[4] M. R. Mokhtar, K. Owens, J. Kwasny, S. E. Taylor, P. A. M. Basheer, D. Cleland, Y. Bai, M. Sonebi, G. Davis, A. Gupta, I. Hogg, B. Bell, W. Doherty, S. McKeague, D. Moore, K. Greeves, T. Sun, K. T. V. Grattan, "Fiber-optic strain sensor system with temperature compensation for arch bridge condition monitoring". *IEEE Sensors J.*, vol. 12, no. 5, pp. 1470–1476. May 2012.

[5] K. T. V. Grattan, T. Sun, "Fiber optic sensor technology: An overview," *Sens Actuators A: Phys*., vol. 82, no. 1–3, pp. 40–61, 2000.

[6] L. Li, L. Xia, Z. Xie, D. Liu, "All-fiber Mach-Zehnder interferometers for sensing applications", *Opt. Express*, vol. 20, no. 10, pp. 11109-11120, May, 2012.

[7] C. Wei, G. Lin, X. Dong and S. Tao, "A tunable polarization-independent comb filter based on high-order mode fiber", *J. Opt*., vol. 15, no. 5, pp. 055403(1)-055403(6), Mar. 2013.

[8] S. M. Tripathi, A. Kumar, R. K. Varshney, Y. B. P. Kumar, E. Marin,and J. -P. Meunier, "Strain and temperature sensing characteristics of single-mode-multimode-single-mode structures," *J. Lightw. Technol.*, vol. 27, no. 13, pp. 2348-2355, Jul. 1, 2009.

[9] S. M. Tripathi, A. Kumar, E. Marin, and J.-P. Meunier, "Critical wavelength in the transmission spectrum of SMS fiber structure employing GeO2-doped multimode fiber," *IEEE Photon. Technol. Lett*., vol. 22, no. 11, pp. 799-801, Jun. 1, 2010.

[10] E. Salik, M. Medrano, G. Cohoon, J. Miller, C. Boyter and J. Koh, "SMS fiber sensor utilizing a few-mode fiber exhibits critical wavelength behavior," *IEEE Photon. Technol. Lett.*, vol. 24, no. 7, pp. 593-595, Apr. 1, 2012.

[11] J. Su, X. Dong, and C. Lu, "Intensity detection scheme of sensors based on the modal interference effect of few mode fiber", *Measurement*, vol. 79, pp. 182-187, Feb. 2016.

[12] J. Su, X. Dong, and C. Lu, "Characteristics of few mode fiber under bending", *IEEE J. Sel. Top. Quant.*, vol. 22, no. 2, pp. 4402307(1)-4402307(7), Jan. 25, 2016.

[13] J. Su, X. Dong, and C. Lu, "Property of bent few-mode fiber and its application in displacement sensor", *IEEE Photon. Technol. Lett*., vol. 28, no. 13, pp. 1387-1390, Jul. 1, 2016.

[14] C. Lu, X. Dong, and J. Su, "Detection of Refractive Index Change from the Critical Wavelength of an Etched Few Mode Fiber", *J. Lightw. Technol.*, vol. 35, no. 13, pp. 2593-2597, Jul. 1. 2017.

[15] C. Lu, J. Su, X. Dong, T. Sun, and K.T.V. Grattan, "Simultaneous Measurement of Strain and Temperature with a Few-Mode Fiber-based Sensor", *J. Lightw. Technol*., vol. 36, no. 13, pp. 2796-2802, Jul. 1. 2018.

[16] Article comprising a dispersion-compensating optical waveguide, by A. M. Vengsarkar, K. L. Walker. (1995, Sep. 5). U. S. Patent No. 5448674 [Online]. Available: https://search.glgoo.com/patents/US5448674

[17] J. Sadeghi, H. Latifi, J. L. Santos, Z. Chenari, F. Ziaee, "Behavior of a hollow core photonic crystal fiber under high radial pressure for downhole application," *Appl. Phys. Lett.*, vol. 104, pp. 071910-1-071910-4, Feb. 2014.

[18] J. Sadeghi H. Latifi, M. Murawski, F. Mirkhosravi, T. Nasilowski, P. Mergo, and K. Poturaj., "Group polarimetric pressure sensitivity of an ellipticalcore side-hole fiber at telecommunication wavelengths," *IEEE J. Sel. Top. Quantum Electron.*, vol. 22, no. 2, pp. 49–54, Mar./Apr. 2016.

[19] A. Kumar, R. K. Varshney, R. Jindal, and S. K. Sharma, "A fiber optic temperature sensor based on LP_{01}-LP_{02} mode interference," *Opt. Fiber Technol*., vol. 6, pp. 83–90, 2000.

[20] A. Kumar, N. K. Goel, and R. K. Varshney, "Studies on a few mode fiber-optic strain sensor based on LP_{01}-LP_{02} mode interference," *J. Lightw. Technol.*, vol. 19, no. 3, pp. 358–362, Mar. 2001.

[21] F. Surre, R.H. Scott, P. Banerji, P. Basheer, T. Sun, K.T. Grattan, "Study of reliability of fibre Bragg grating fibre optic strain sensors for field-test applications," *Sensor Actuators, A*, vol. 185, no. 5, pp. 8-16, Oct. 2012.

[22] J. Sadeghi, A. H. Ghasemi, and H. Latifi, "A label-free infrared opto-fluidic method for real-time determination of flow rate and concentration with temperature cross-sensitivity compensation," *Lab Chip*, vol. 16, pp. 3957– 3968, 2016.